

Supporting information for “Frequency-Controlled Electrophoretic Mobility of a Particle within a Porous, Hollow Shell”

Tom A.J. Welling¹, Albert Grau-Carbonell¹, Kanako Watanabe², Daisuke Nagao², Joost de Graaf³, Marijn A. van Huis¹, and Alfons van Blaaderen¹

¹Soft Condensed Matter, Debye Institute for Nanomaterials Science, Utrecht University, Princetonplein 5, 3584 CC Utrecht, The Netherlands

²Department of Chemical Engineering, Tohoku University, 6-6-07 Aoba, Aramaki-aza, Aoba-ku, Sendai 980-8579, Japan

³Institute for Theoretical Physics, Center for Extreme Matter and Emergent Phenomena, Utrecht University, Princetonplein 5, 3584 CC Utrecht, The Netherlands

1 Details of the Finite-Element Calculations

We performed finite-element calculations using the COMSOL 5.4 Multi-Physics Modeling Software. We set up a system with a spherical core particle having a radius of 170 nm. A hollow shell with an inner radius of 370 nm and shell thickness of 40 nm surrounded it with the core particle positioned at the center of the shell. The sizes of the core particle and shell were based on the dimensions of the particles used in experiments, which were synthesized via the method of Watanabe and coworkers.¹ The sphere and shell were located on the symmetry axis of a cylindrical fluid domain with a height and width of 5 μm . The core particle is allowed to move through the shell due to electric and viscous forces acting upon it. Here we describe the boundary conditions in more detail. We also explain the moving core particle and the mesh during the calculation, and the solver settings.

1.1 Boundary Conditions

Figure S1 shows an overview of the boundary conditions used for each equation that was solved, namely the Poisson equation, the Nernst-Planck equation and the Stokes equation for an incompressible fluid. The relevant values for the quantities discussed next are provided in Tables S1 and S2.

1.1.1 The boundary conditions for the Poisson equation.

The left panel in Figure S1 shows the relevant boundary conditions. The right boundary of the simulation box carries no charge ($\hat{n} \cdot \nabla \phi = 0$), where \hat{n} is the unit normal to the surface and ϕ is the electric potential). The lower, red boundary has an applied voltage, whereas the upper, blue boundary is grounded. This setup allowed us to apply an external field with minimal effect of the finite size of the calculation volume. The outer box in the calculation was 5 times larger than shown in Figure S1. All domains have a relative permittivity ϵ_r (see Table S1). Domains with free charges also have a local charge density ρ_c , which is given by the local abundance of ions $\rho_c = N_A e (z_+ c_+ + z_- c_-)$. Here N_A is Avogadro’s constant, e the electron charge, z_+ and z_- the charge numbers of the ionic species, and c_+ and c_- the local concentration of the ionic species. The surfaces of the core and the shell carry a charge density σ (see Table S2).

1.1.2 The boundary conditions of the Nernst-Planck equations.

The middle panel in Figure S1 shows the relevant boundary conditions. The outer boundaries of the simulation box are held at a constant ion concentration, which means that these regions serve as a reservoir. The fluid has a temperature T and the two types of ions, positive and negative, have diffusion coefficients D_{pos} and D_{neg} , respectively. The ion diffusion coefficients within the silica shell wall $D_{s,j}$ are lower than bulk diffusion coefficients ($D_{s,j} = \Phi_p D_j$), with Φ_p the porosity. The boundary of the core has a no-flux boundary condition ($\hat{n} \cdot (\mathbf{J}_j + \mathbf{u}c_j) = 0$), where \mathbf{u} is the flow velocity and c_j represent the local ion concentrations; \mathbf{J}_{\pm} indicates the associated fluxes. There is an open boundary for ions to go through on the shell walls.

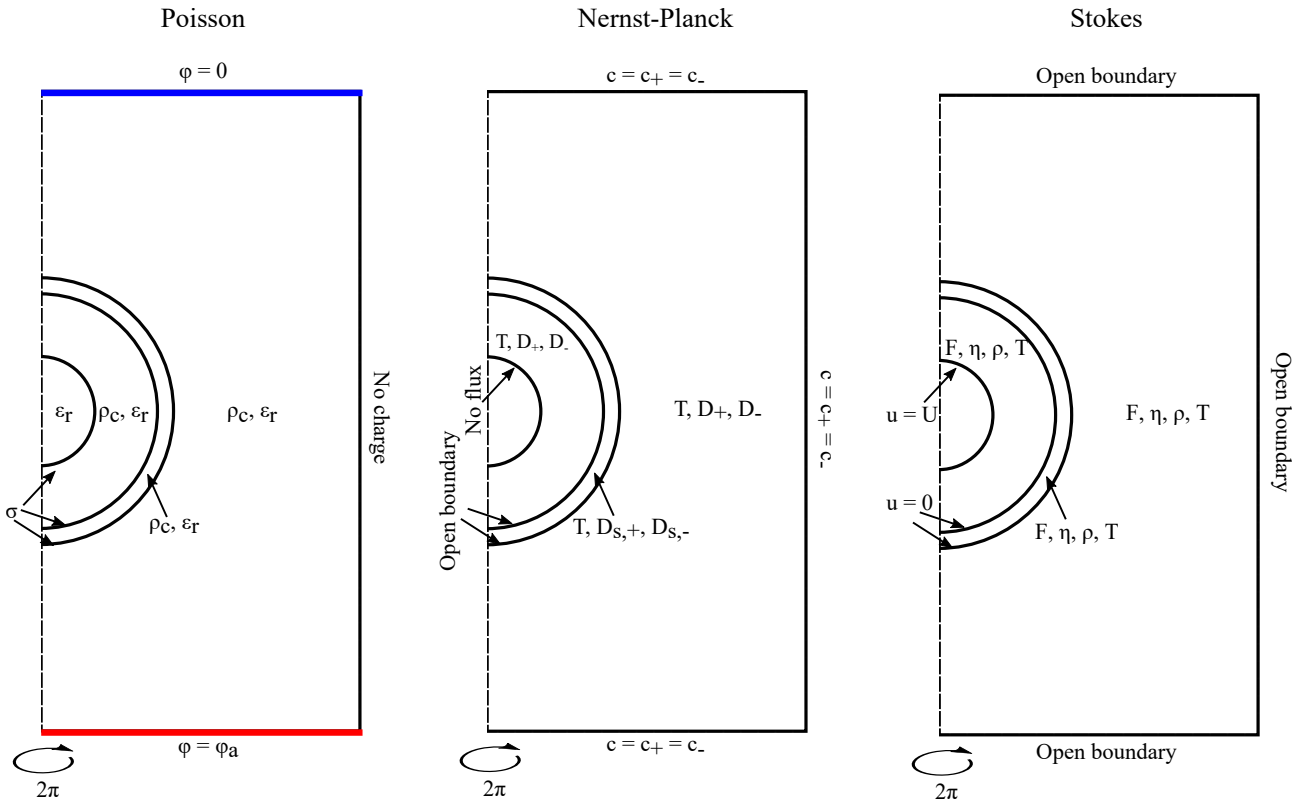


Figure S1: Boundary conditions used for the yolk-shell geometry used in the 2D axisymmetric finite-element calculations.

1.1.3 The boundary conditions for the Stokes equations.

The right panel in Figure S1 shows the relevant boundary conditions. The outer boundaries of the simulation box are open boundaries ($(-p\mathbf{I} + \eta(\nabla\mathbf{u} + (\nabla\mathbf{u})^T))\hat{n} = 0$). The shell walls have no-slip boundary conditions $\mathbf{u} = \mathbf{0}$. The core particle moves with a velocity calculated from the electric and hydrodynamic forces acting on it as described in the Methods section. The fluid has a density ρ_{fluid} , a viscosity η , a temperature T and a volume force $\mathbf{F} = -eN_A(c_+ + c_-)\nabla\phi$.

1.2 Moving Core Particle and Mesh

The rotational symmetry of the system was exploited by performing 2D axisymmetric calculations to minimize the number of elements required. We used local refinement with small elements in the areas of the double layers as shown in Figure S2. The thickness of the refined elements was approximately the same as the Debye length. It is more common to apply a thicker area of refined elements,²⁻⁴ but this was not possible here due to the core being able to approach the shell more closely than two Debye lengths. As we wanted to keep the area of refined elements the same during the whole simulation, these areas had to be less thick. We compensated for the thinner area of refined elements by putting more mesh elements in these areas than is common practice, and also made sure that the elements did not expand too quickly when moving away from these dense mesh areas. However, the size of the elements was allowed to expand radially outward from the double layers (by a factor 1.25, up to a maximum element size of 15 nm).

The core particle could move along the symmetry axis. We determined its velocity \mathbf{U} via the electric force \mathbf{F}_e and the hydrodynamic drag force \mathbf{F}_h acting on it via Newton's second law of motion⁵

$$\mathbf{F}_e + \mathbf{F}_h = \frac{4}{3}\pi a^3_{\text{particle}}(\rho_{\text{particle}} - \rho_{\text{fluid}})\frac{d\mathbf{U}}{dt}, \quad (1)$$

where ρ_{particle} and ρ_{fluid} are the density of the particle and fluid, respectively. The electric force and hydrodynamic drag force were obtained by integrating the electric and hydrodynamic stress tensors over the surface of the particle, respectively.

$$\mathbf{F}_h = \oint_S \mathbf{T} dS \quad (2)$$

$$\mathbf{F}_e = \oint_S \mathbf{M} dS \quad (3)$$

Core particle radius a_{particle}	170 nm
Inner shell radius a_{shell}	370 nm*
Shell thickness t_{shell}	40 nm*
Shell porosity Φ_p	0.01 – 1
Fluid viscosity η	1 mPa s
Fluid density ρ_{fluid}	10^3 kg m^{-3}
Temperature T	293.15 K
Particle density ρ_{particle}	$2 \cdot 10^3 \text{ kg m}^{-3}$
Fluid relative dielectric constant $\epsilon_{r,\text{fluid}}$	78.4
Particle relative dielectric constant $\epsilon_{r,\text{particle}}$	3.8
Shell relative dielectric constant $\epsilon_{r,\text{shell}}$	$(1 - \Phi_p) \epsilon_{r,\text{particle}} + \Phi_p \epsilon_{r,\text{fluid}}$
Positive ion diffusion coefficient D_-	$1.022 \cdot 10^{-9} \text{ m}^2 \text{ s}^{-1}$
Negative ion diffusion coefficient D_+	$2.037 \cdot 10^{-9} \text{ m}^2 \text{ s}^{-1}$
Ion diffusion coefficient in shell $D_{s,j}$	$\Phi_p D_j$
Positive ion charge number z_+	1
Negative ion charge number z_-	-1
Ionic strength I	2 mM**
Core particle surface charge density σ_{particle}	$-6.3 \cdot 10^{-3} \text{ C m}^{-2}$ **
Inner & outer shell surface charge density σ_{shell}	$-6.3 \cdot 10^{-3} \text{ C m}^{-2}$ **
Length of simulation box	5 μm
Voltage V	0.5 V
Frequency f	1 – 100 kHz

Table S1: Typical values for a finite-element calculation. *For the larger shell: $a_{\text{shell}} = 496 \text{ nm}$ $t_{\text{shell}} = 55 \text{ nm}$. ** The values here are for 2 mM salt. In Table S2 we give the values for other salt concentrations.

I	0.002 mM	0.2 mM	2 mM	25 mM
σ_{particle}	$-0.18 \cdot 10^{-3} \text{ C m}^{-2}$	$-2.1 \cdot 10^{-3} \text{ C m}^{-2}$	$-6.3 \cdot 10^{-3} \text{ C m}^{-2}$	$-22.1 \cdot 10^{-3} \text{ C m}^{-2}$
σ_{shell}	$-0.095 \cdot 10^{-3} \text{ C m}^{-2}$	$-2.1 \cdot 10^{-3} \text{ C m}^{-2}$	$-6.3 \cdot 10^{-3} \text{ C m}^{-2}$	$-22.1 \cdot 10^{-3} \text{ C m}^{-2}$

Table S2: Surface charge densities of the core particle and shell for different salt concentrations.

The particle position was then updated by multiplying the velocity per timestep and the timestep itself. The backward differential formula (BDF) method uses non-uniform steps in time to solve the physics for each time step. When the mesh in the blue region in Figure S2 became too distorted, it was updated to ensure accurate reproduction of the physics. This was whenever the following criterion was met:

$$\frac{\text{tr}F^T F}{2J^{2/n}} - \frac{n}{2} > 0.5, \quad (4)$$

where F is the deformation gradient, J its determinant, and n is the space dimension. The internal COMSOL name for this quantity is "comp1.spatial.lisoMax".

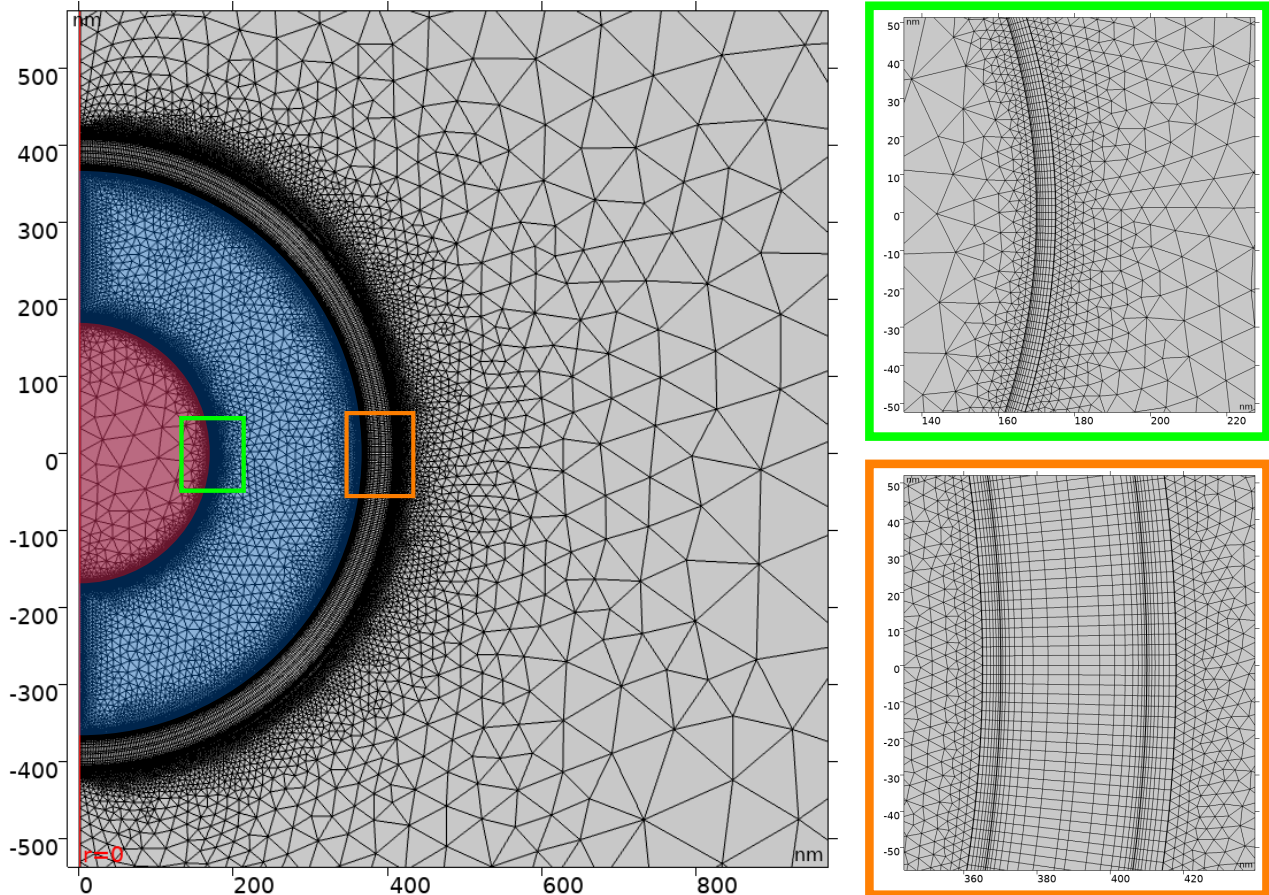


Figure S2: Example of the mesh of the yolk-shell geometry used in the 2D axisymmetric finite-element calculations. The mesh near the surfaces, at the double layers, is extra refined to deal with large changes in concentration and potential over a small length. The mesh of the red domain was moved according to the updated particle position. The mesh of the blue domain was automatically updated when it became too deformed.

We first performed a stationary study with a shell that was open to ions and for which no electric field was applied. During this study the equilibrium double layers could form. This solution was used as an initial configuration to perform the time-dependent calculation with the AC electric field. For this calculation the shell was given a fixed porosity which determined how fast ions diffused through the shell, according to the rules in Table S1. In the time-dependent solver using the BDF method a relative tolerance of 0.01 was used. This controls the relative error in each time step. An absolute tolerance factor of 0.5 is applied to scaled variables to control the absolute error. The time step taken by the solver was allowed to vary up to a maximum of $1/f/100$, where f is the frequency. Furthermore, backward Euler consistent initialization was used. To solve the system at a certain time step we used a fully coupled solver, with MUMPS as the direct solver for the linear equations.

1.3 Model Verification

In order to ensure that our finite-element model provided acceptable results for the electrophoresis of a particle, we compared results of our model without the shell with established literature values.^{5,6} First, we compared the stationary electrophoretic velocity from our simulations to the work of O'Brien and White.⁶ For these calculations we used a constant potential boundary condition to be as close to their conditions as possible. The electric field strength was set to 100 V m^{-1} to be in the regime of low electric field. The results are shown in

Figure S3a, which shows good agreement with the work of O'Brien and White.⁶ Note that in the calculations in this work the scaled zeta potential is 2. Second, we compared the dynamic electrophoretic velocity under an AC electric field to the work of Eric Lee.⁵ For these calculations we used constant surface charge boundary conditions, as these are also used in the simulations on the yolk-shell system in this work. The electric field strength was set to 100 V m^{-1} to be in the low-field regime. The results of these calculations also agree well with the work of Lee (Figure S3b).⁵

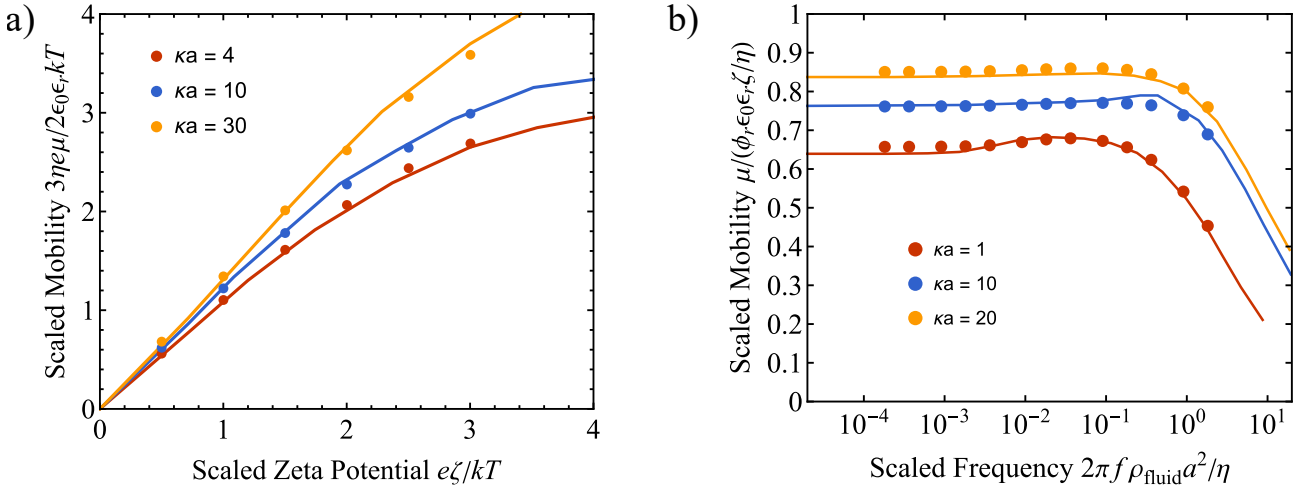


Figure S3: Model verification. a) Results of finite-element calculations of the stationary electrophoretic mobility for various surface potentials and salt concentrations compared to the work of O'Brien and White (solid lines).⁶ b) Results of finite-element simulations of the dynamic electrophoretic mobility for various salt concentrations and frequencies (scaled surface potential $\phi_r = 2$) compared to the results of Eric Lee (solid lines).⁵

1.4 Mesh Refinement

We verified that we had used a sufficiently dense mesh in the areas where this mattered as follows. We made the mesh in the EDL regions 4, 9, and 16 times more dense and ran the simulations for a shell with 100% porosity at 100 V mm^{-1} and 100 kHz . No changes in the electrophoretic velocity of the core particle was observed.

2 Synthesis, Zeta Potential, Etching and Overgrowth of Yolk-Shell Particles

For the synthesis of the original rattle particles the reader is referred to our previous collaborative work.¹ The zeta potential of the core particles was measured to be -41 mV in aqueous solution for the same sample used in this study.¹ To determine the zeta potential of the core, the as-prepared core particles were overgrown with the sacrificial polystyrene layer. They were then calcinated to remove the polystyrene layer. This allows us to measure the zeta potential of the cores that have been through the same treatment as the cores within the yolk-shell geometry. We furthermore measured the zeta potential of the shells of the as-prepared particles and it was found to be $-45 \pm 7 \text{ mV}$ in aqueous solution (2 mM LiCl). However, realistically we do not know the zeta potential of the inner part of the shell (we cannot measure it) and it is likely that the zeta potentials of the core particles may deviate somewhat when they are in the shells. By mechanically cracking the shells it may be possible to measure the zeta potential of the cores in the future. As such, we decided to use the same surface charge density for all silica surfaces in the simulations, leading to -50 mV surface potential for the core and -40 mV surface potential for the shell.

The procedure to grow silica on top of the shell of the original rattle particles is as follows (Figure S4). An aqueous suspension of the rattle particles was mixed with an ethanol solution. The volume fraction of water in ethanol was 0.25, and the total volume of the mixture was 10 mL . After stirring for 5 min at 35°C , $100 \mu\text{L}$ of 100 mM NaOH ($\geq 98.0\%$, Sigma-Aldrich) aqueous solution was added to the mixture. An ethanol solution of tetraethyl orthosilicate (TEOS, $\geq 98.0\%$, Sigma-Aldrich) ($56 \mu\text{L}$, 1.8 M) was injected three times with intervals of 45 minutes. The total concentration of TEOS was 30 mM . The reaction was conducted under stirring at 35°C overnight. The obtained particles were centrifuged twice with ethanol and with water.

The procedure to etch the shells of the original rattle sample is as follows (Figure S5). An aqueous solution of NaOH (100 mM , $287 \mu\text{L}$) was added to 8.7 mL of the dispersion of rattle particles. The mixture was stirred at 40°C for 7 hours. The solution pH of the mixture was 11.5. The etched particles were centrifuged twice with water, and redispersed in water.

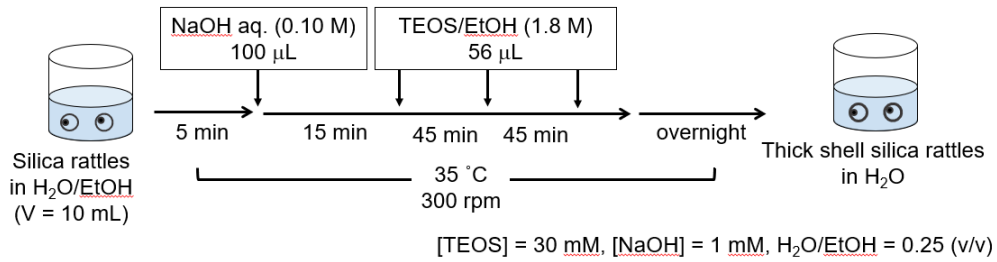


Figure S4: The procedure for overgrowing the shells of the rattle particles.

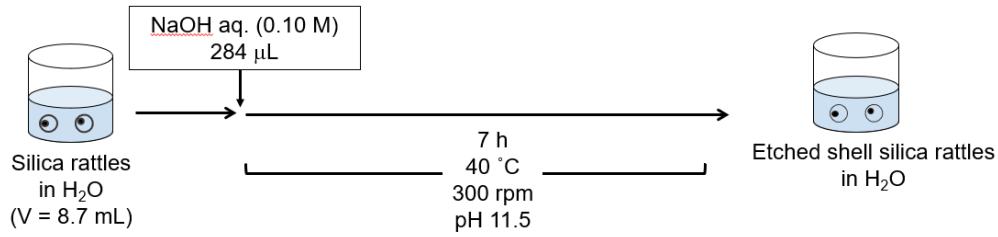


Figure S5: The procedure for etching the shells of the rattle particles.

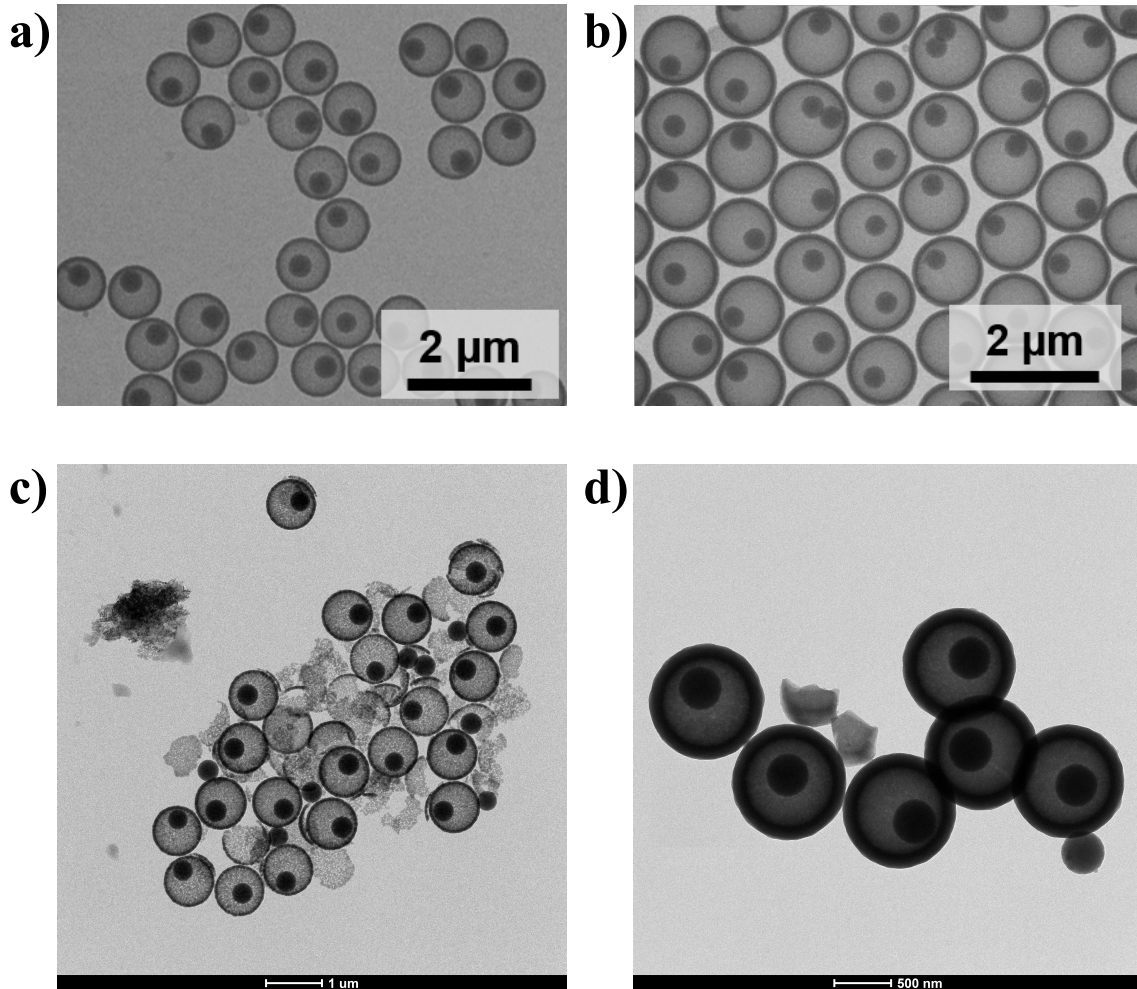


Figure S6: Bright-field TEM images of the four different kinds of rattle-type particles used in this study. a) Silica rattles with a small shell ($a_{\text{shell}} = 370$ nm), b) silica rattles with a large shell ($a_{\text{shell}} = 496$ nm), c) silica rattles with a small shell that is etched more significantly, d) silica rattles with a small shell that is overgrown with silica.

3 A Closer look at the Electric Field inside the Liquid Cell and within the Rattle Geometry

Figure S7 shows the electric field in a 3D environment resembling the liquid-cell geometry in the experiments, where we solved the Poisson equation. The area with water ($\epsilon_r = 78.4$) was 100 by 50 by 2 micron. In this

calculation we placed 200 nm thick SiN windows ($\epsilon_r = 9.5$) on the top and the bottom of the water layer. The electrodes were 50 by 5 by 0.075 micron. The middle of the electrodes were spaced $30 \mu\text{m}$ apart. The height of the liquid cell and thus the water layer within was taken to be $2 \mu\text{m}$ in this calculation. One electrode was given a constant potential boundary condition of 3 V, while the other was given a ground boundary condition (0 V). The edges of the calculation volume were assumed to have zero charge. It was found that the electric field between the two electrodes was at least 95 V mm^{-1} in the area between the electrodes where the recordings of the yolk-shell particles were done. The electric field did not vary significantly with the z height. We thus expect less than a 5% error in the electric field in our experiments.

We also calculated what the effect of the dielectric constant of the shell was on the electric field within the yolk-shell geometry. Figure S8 shows the field in and around the yolk-shell geometry upon application of a 100 V mm^{-1} electric field. A drop of 21% to an average electric field of 79 V mm^{-1} was observed for a shell thickness of 40 nm and a shell dielectric constant of $\epsilon_r = 11.3$, which corresponds to a shell porosity of 10%.

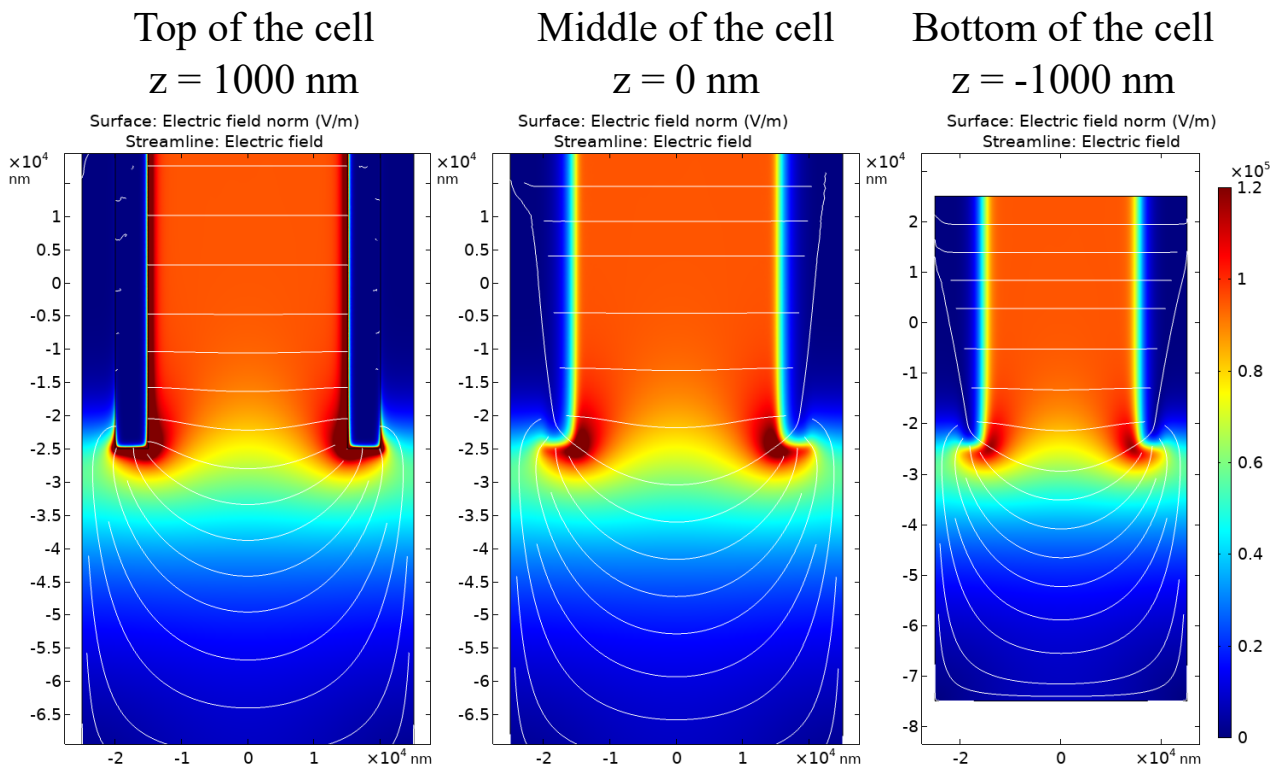
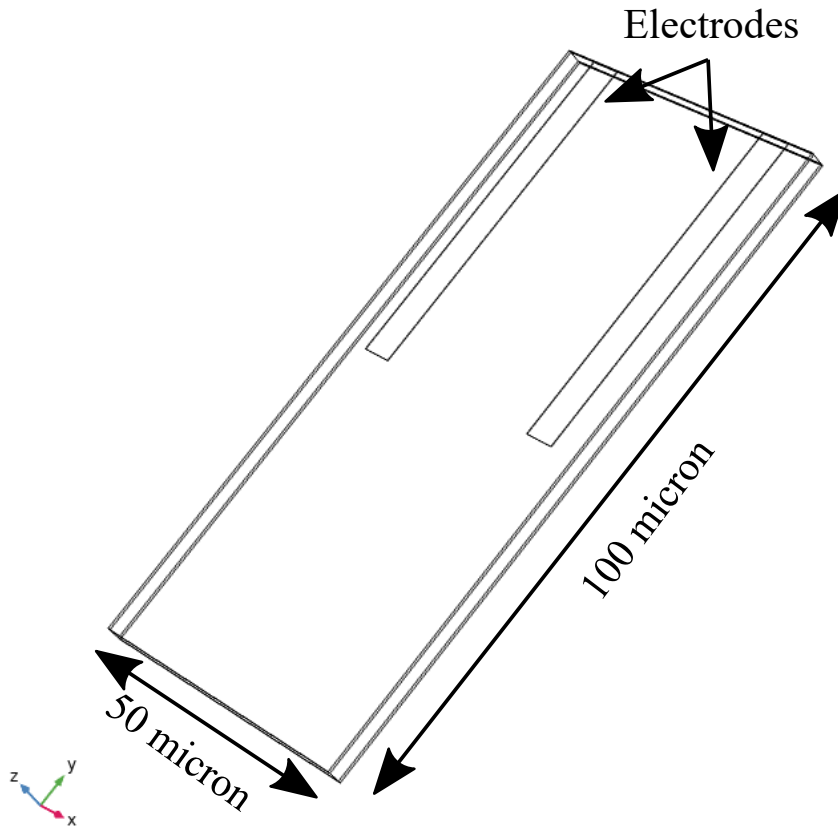


Figure S7: Electric field within a liquid cell geometry calculated by solving the Poisson's equation for a geometry resembling the liquid cell, where the electrodes are spaced $30 \mu\text{m}$ apart. The color scale indicates the strength of the electric field.

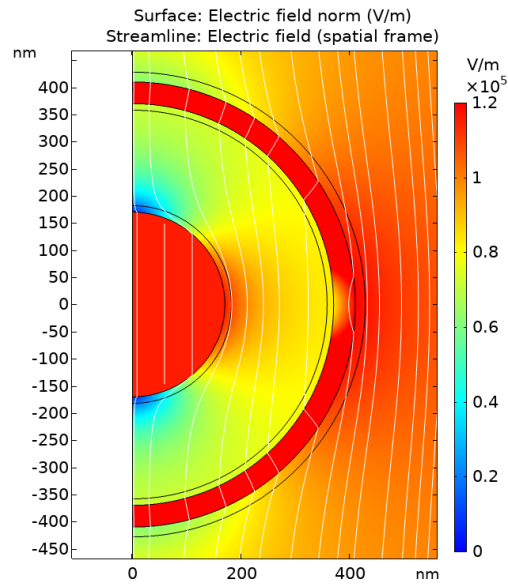


Figure S8: Electric field drop within the rattle geometry by only taking the dielectrics of the shell into account. For this calculation we solved only the Poisson equation to estimate the electric field reduction within the yolk-shell geometry without taking ions and their movement through the shell into account. The dielectric constant of the shell was the same as those in the full calculations with a porosity of the shell of 10%: $\epsilon_r = 11.3$. The surface potential of the core is -50 mV, and that of the shell is -40 mV.

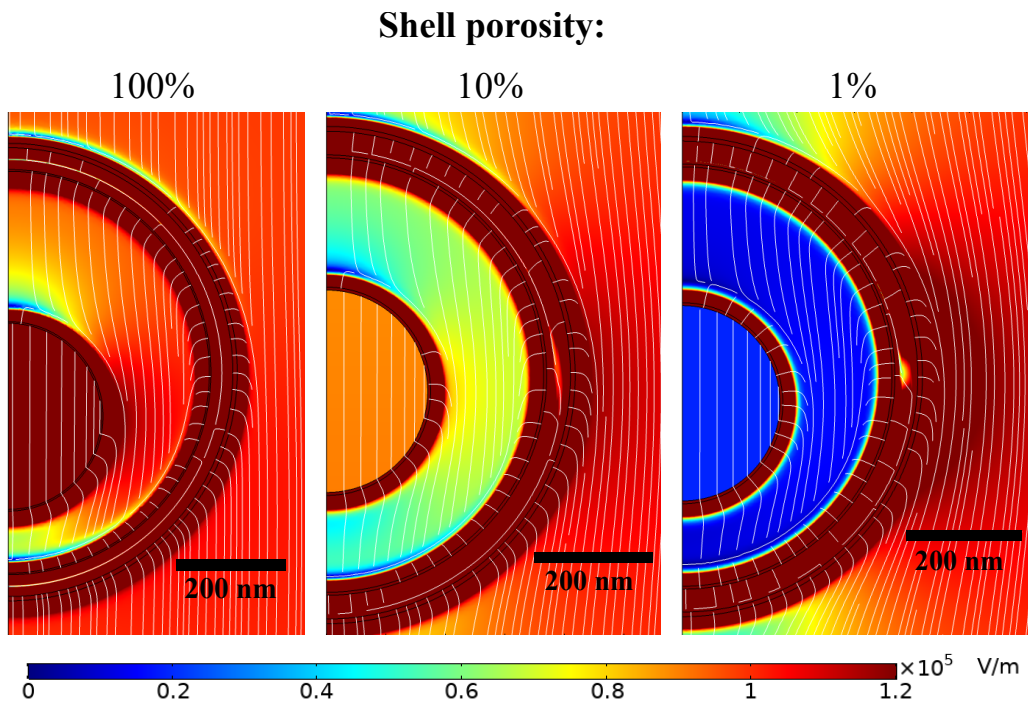


Figure S9: Electric field strength within the rattle geometry at the maximum of the electric field sine wave (at 4.5π , so after 2.25 cycles) for different porosities of the shell (as indicated by the percentages in the subfigure titles). The surface potential of the core is -50 mV, and that of the shell is -40 mV.

4 Supporting Figures

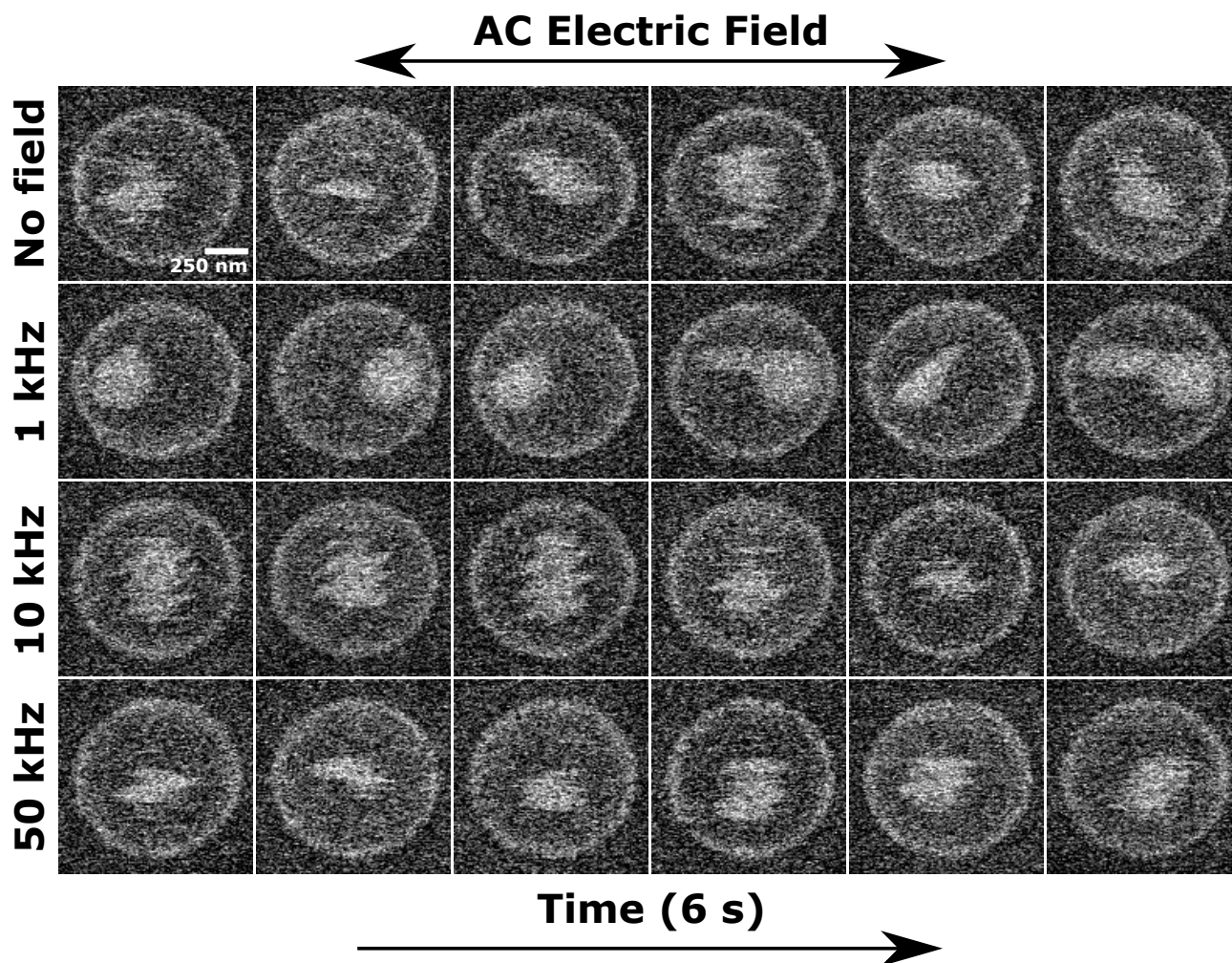


Figure S10: Frequency-dependent mobility of a core particle within a shell under application of a 100 V mm^{-1} AC electric field in aqueous solution of 2.00 mM LiCl . The electron dose rate was $45 \text{ e}^{-} \text{ nm}^{-2} \text{ s}^{-1}$. For each frequency, six consecutive frames are shown with a frame time of 1 s . While at lower frequencies the core moves parallel to the electric field, at intermediate frequencies the core moves orthogonal to the electric field. At high frequencies, there is no significant influence of the electric field.

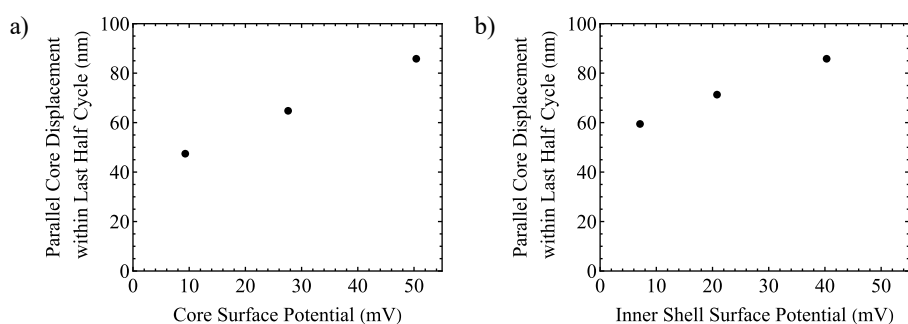


Figure S11: Calculated effect of the surface potential on the core particle and the shell on the displacement of the core particle. a) Core displacements as function of the core surface potential. The inner shell surface potential was -40 mV . b) Core displacements as function of the inner shell surface potential. The core surface potential was -50 mV . The other parameters are the same as Figure 3 of the main text.

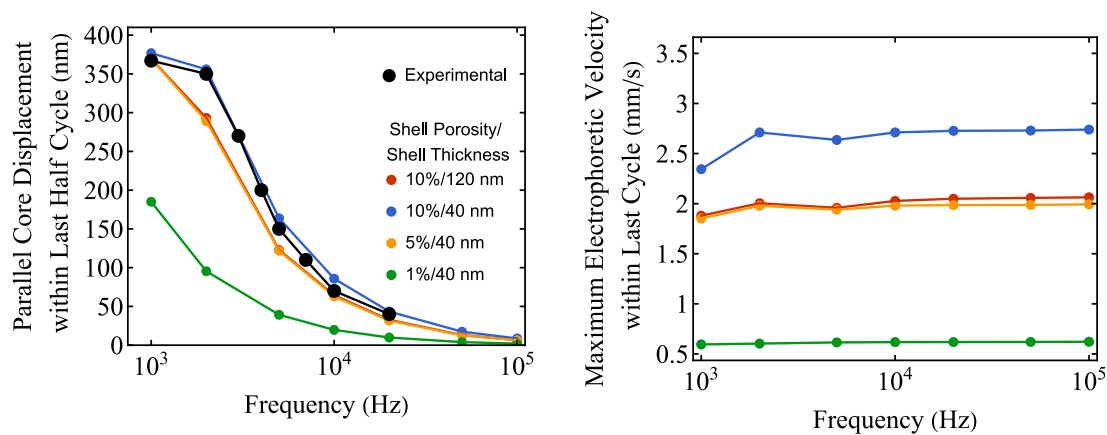


Figure S12: Calculated effect of the thickness of the shell on the displacement and velocity of the core particle. A 120 nm thick shell with 10% porosity has a similar effect on the particle velocity as a 40 nm thick shell with 5% porosity. The other parameters are the same as Figure 3 of the main text.

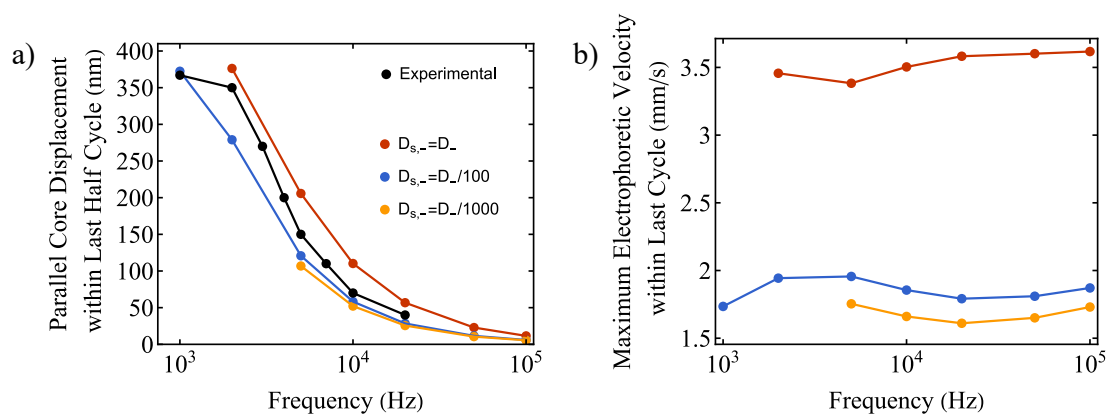


Figure S13: Calculated effect of the diffusion coefficient of the negative ion through the shell on the displacement and velocity of the core particle. The dielectric constant of the shell was 78.4 and $D_{s,+} = D_+$. The other parameters are the same as Figure 3 of the main text.

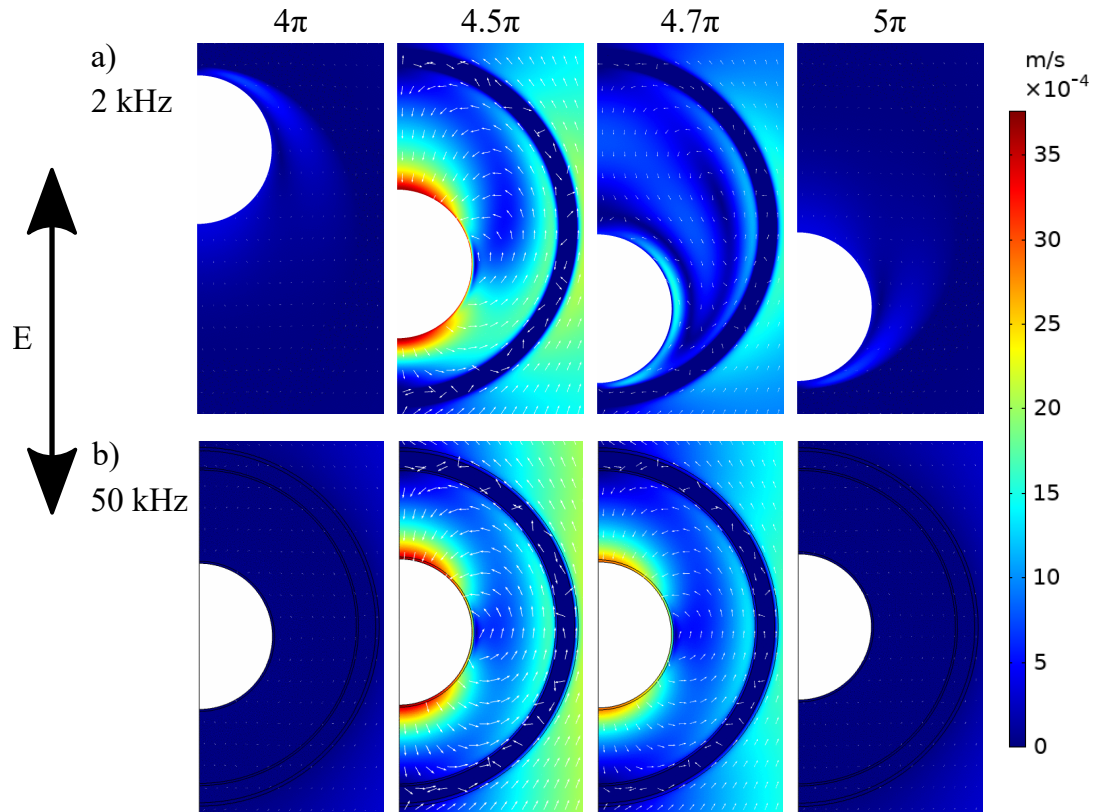


Figure S14: Calculated flow profiles for a yolk-shell geometry for a shell with 100% porosity during the application of a 100 V mm^{-1} AC electric field of 50 and 2 kHz. The first image is after 2 cycles of the electric field and the images that follow are all within half an electric field cycle (phase 4π to 5π). It can be seen that the flow originating from the EDL on the inner shell wall contributes positively to the velocity of the particle. For 2 kHz the flow profile is different, as the particle moves significantly during the electric field cycle. The surface potential of the core is -50 mV , and that of the shell is -40 mV .

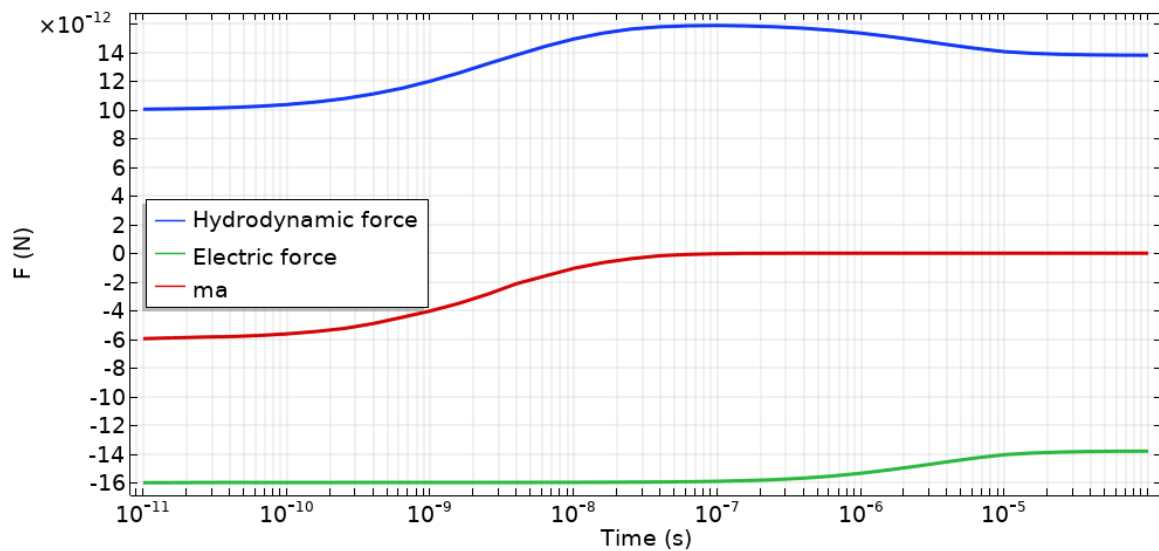


Figure S15: The electric force, hydrodynamic force and the acceleration term as function of time for a free particle ($a_{\text{particle}} = 170 \text{ nm}$, $\kappa a = 1$) when applying a constant electric field of 100 V mm^{-1} . It shows that for the times relevant in our system using an AC electric field with frequencies of 100 kHz or lower, the acceleration term is negligible.

References

- ¹ Watanabe, K.; Ishii, H.; Konno, M.; Imhof, A.; van Blaaderen, A.; Nagao, D. Yolk/Shell Colloidal Crystals Incorporating Movable Cores with Their Motion Controlled by an External Electric Field. *Langmuir* **2017**, *33*, 296–302.
- ² Rempfer, G.; Davies, G. B.; Holm, C.; De Graaf, J. Reducing Spurious Flow in Simulations of Electrokinetic Phenomena. *Journal of Chemical Physics* **2016**, *145*.
- ³ Rempfer, G.; Ehrhardt, S.; Holm, C.; de Graaf, J. Nanoparticle Translocation through Conical Nanopores: A Finite Element Study of Electrokinetic Transport. *Macromolecular Theory and Simulations* **2017**, *26*, 1–14.
- ⁴ Welling, T. A. J.; Watanabe, K.; Grau-Carbonell, A.; de Graaf, J.; Nagao, D.; Imhof, A.; van Huis, M. A.; van Blaaderen, A. Tunability of Interactions between the Core and Shell in Rattle-Type Particles studied with Liquid-Cell Electron Microscopy. *ACS Nano* **2021**, *15*, 11137–11149.
- ⁵ Lee, E. Dynamic Electrophoresis of Rigid Spherical Particles. *Interface Science and Technology* **2019**, *26*, 123–142.
- ⁶ O'Brien, R. W.; White, L. R. Electrophoretic Mobility of a Spherical Colloidal Particle. *Journal of the Chemical Society, Faraday Transactions 2: Molecular and Chemical Physics* **1978**, *74*, 1607–1626.